

What it takes to measure reionization with fast radio bursts

Stefan Heimersheim¹, Nina Sartorio¹, Anastasia Fialkov^{1,2}, and Duncan R. Lorimer^{3,4}

¹*Institute of Astronomy, University of Cambridge, Madingley Road, Cambridge CB3 0HA, UK*

²*Kavli Institute for Cosmology, Madingley Road, Cambridge CB3 0HA, UK*

³*West Virginia University, Department of Physics and Astronomy, P. O. Box 6315, Morgantown, WV, USA*

⁴*Center for Gravitational Waves and Cosmology, West Virginia University, Chestnut Ridge Research Building, Morgantown, WV, USA*

August 2, 2021

Fast radio bursts (FRBs) are extra-galactic radio transients which, owing to the observed dispersion of the signal, can be used as cosmological probes. In this Letter we use high redshift FRBs to constrain the history of hydrogen reionization and measure the reionization optical depth τ . For the first time, we do so in a model-independent way by using a free-form parameterization of the reionization history. In a Bayesian analysis we find that 100 localized FRBs, produced during the first billion years of cosmic history (redshifts $z > 5$), are required to surpass the measurement by the *Planck* satellite, constraining τ to an accuracy of 11% (at 68% confidence) and the midpoint of reionization to 6%, while 1000 FRBs would further tighten these constraints to 9% and 3% accuracy respectively.

Introduction A new type of radio transient signals, called Fast Radio Bursts (FRBs), is one of the unsolved mysteries in astronomy. The quest for understanding their origins is ongoing, and, since the discovery of the very first FRB in 2007 [1], a few hundreds such signals have been detected by the most sensitive radio telescopes [2–5].

These signals are significantly dispersed by the ionized medium distributed along the path between the sources and the observer. Since the observed dispersion, quantified in terms of dispersion measure (DM), is much larger than the contribution of our local environment, it is now known that the overwhelming majority of FRBs are of extra-Galactic origin. For the bulk of the detected FRBs the large fraction of DM is due to the free electrons found in the intergalactic medium [IGM, 6, 7], with a lesser contribution from the FRB host environment and the Milky Way. Dependence of DM on the cosmological redshift, z , of the FRB hosts may shed light on properties of the IGM [8–10] and can be used to measure cosmological parameters [5, 10–19]. For instance, using a sample of observed low-redshift FRBs ($z \lesssim 0.66$), Macquart *et al.* [10] demonstrated that these signals are sensitive to the total baryon fraction along the line of sight and, thus, can help solving the missing baryon problem by counting the total number of baryons in the IGM.

Existing data imply that the number of FRBs traces the star formation rate [SFR, 20, 21], suggesting that a population of FRB progenitors could exist beyond the current observational cutoff at $z \sim 3$ [22]. It is yet unknown when the first star forming objects, potential progenitors of the earliest FRBs, might have formed. Theoretical models predict an early onset of star formation with the first stars in the observable Universe ap-

pearing just a few tens of million years after the Big Bang [23]. On the other hand, observations of high-redshift galaxies find evolved and luminous objects including a bright galaxy at $z \sim 11$ detected by the Hubble Space Telescope [HST, 24] and a metal-rich galaxy at $z \sim 9.1$ observed by the Atacama Large Millimeter/submillimeter Array, HST and *Spitzer* whose existence requires star formation to begin at $z \gtrsim 15$ [25]. Therefore, if the correlation between SFR and the number of FRBs holds for the entirety of cosmic history, it is possible that sensitive telescopes such as the future Square Kilometre Array (SKA) will see a multitude of FRBs originating from high redshift galaxies [e.g., 26, 27].

The exact expected number of high redshift FRBs is uncertain as both the FRB luminosity function and the nature of FRB progenitors are poorly understood and might change as stellar populations evolve. The recent detection of a Galactic FRB 200428 associated with magnetar SGR 1935+2154 [4, 28] suggests that at least some FRBs are related to highly magnetized neutron stars. However, the ambiguity remains as there are multiple channels through which a magnetar could give rise to an FRB [29–34]. Moreover, magnetar formation itself is still an open question [35, 36] and it is yet unknown how the abundance of magnetars changes in the course of cosmic history. One possibility is that magnetars [37–42], or even FRBs themselves [38, 43–47], result from stellar mergers. In this case the expected number of high-redshift FRBs would strongly depend on the highly uncertain initial mass function of the first generations of stars [48–52].

From the observational point of view, detecting high redshift FRBs beyond the current limit of $z \sim 3$ requires both, sufficient telescope sensitivity and a capability to detect highly dispersed events. Some of the existing telescopes already have these specifications, including the Five-hundred-meter Aperture Telescope (FAST) which could detect the brightest FRBs up to $z \sim 10$ [53]. The Green Bank Telescope (GBT) can detect FRBs at similar redshifts carrying out a high-sensitivity search using the GREENBURST experiment [54]. (Although on their own these telescopes will not be able to localize FRBs.) Next generation telescopes such as SKA will be able to detect multiple FRBs per day originating at high redshifts [12, 55] and it has the potential of detecting the brightest FRBs from the first billion years of cosmic history [12, 55].

If detected, high redshift FRBs will be extremely rewarding in terms of the science they deliver. First, either detection or non-detection of these events would probe progenitor theories

and would, thus, act as an indirect probe of star formation at high redshifts. Second, high-redshift FRBs are expected to be sensitive cosmological probes. Theoretical predictions show that a population of FRBs at $z \sim 3 - 4$ could be used to probe second helium reionization happening around redshift $z \approx 3.5$ [56–60], while signals from $z > 5$ would primarily trace variation in the ionization state of hydrogen atoms, and, consequently, could be used to probe the Epoch of Reionization [EoR, 12, 61–65]. Such measurements would help to constrain the total optical depth of the Cosmic Microwave Background (CMB), τ , to a higher accuracy than what is presently achievable [12, 61–63].

Current best limits on τ have a large uncertainty of more than 10% and represent a hurdle for precision cosmology. These limits are derived from the CMB [Planck 2018 results, 66, hereafter Planck18] which is affected by the EoR as photons scatter off the ionized gas. The signature of the EoR in the CMB is degenerate with the initial amplitude of curvature perturbations A_s [67], and, thus, the poor precision in τ also degrades the estimates of the primordial power spectrum. Another quantity that suffers from the poor estimate on τ is the sum of neutrino masses, Σm_ν , extracted from a joint analysis of the CMB and Large Scale Structure [68]. A more accurate measurement of τ is, therefore, expected to improve our fundamental understanding of the Universe¹.

Although the importance of high-redshift FRBs as the EoR probes has been praised in literature [12, 62–65], existing works² make assumptions that either lead to biases in the results or limit the constraining power of the data. Fialkov & Loeb [12] were the first to point out that FRBs could be used as precision probes of the EoR and performed a simplified error analysis to estimate the expected accuracy on τ (a similar analysis was performed by Beniamini *et al.* [62]), which stimulated further studies. Beniamini *et al.* [62] and Hashimoto *et al.* [64] constrain the ionized fraction by grouping FRBs into redshift bins and considering the difference between neighboring DM bin-averages. As a result of binning, redshifts and DMs of the individual FRBs are lost and with them the capabilities to smoothly trace the EoR. Furthermore, in the absence of a functional form for the reionization history, this approach does not permit imposing global relationships (such as the monotonicity of the reionization history) across large redshift ranges. Another approach was taken by Zhang *et al.* [63] and Pagano & Fronenberg [65] who postulate a specific shape of the reionization history, either the popular tanh function or a simulation-based form. Because the actual EoR history is unknown, such assumptions lead to biased results. In order to demonstrate the limitation of the latter approach, we use our synthetic data (described below and in Section A.1) to derive reionization constraints assuming the widely adopted tanh model [e.g. 63]. We find that fixing the reionization history to the symmetric tanh function, parameterized by the duration and midpoint of the EoR, underestimates the value of τ by $\sim 10\%$, excluding the true value at high confidence (99%). The tanh model enforces a symmetric reionization history so that a potential high-redshift

¹A similar goal can be achieved with future radio experiments measuring the redshifted 21 cm line of neutral hydrogen in the IGM [69]; however, the 21-cm signal is sensitive to a combination of thermal and reionization histories and extra care should be taken to remove this degeneracy when constraining the EoR [70].

²Note that here we only consider methods based on localized FRBs.

contribution is systematically underestimated. For the specific synthetic data used here, the asymmetric model of Dai & Xia [61] yields better constraints on the EoR but still significantly underestimates τ .

In this Letter we adopt a model-independent approach and, for the first time, use it to constrain the full shape of the reionization history as well as the optical depth τ . This method allows surpassing the accuracy of the-state-of-the-art CMB experiments in constraining the EoR and τ while avoiding the pitfalls of commonly used techniques.

Methods Our reionization constraints rely on measuring the DMs and source redshifts of high- z FRBs. In order to test our method, we generate two synthetic FRB data sets with 100 and 1000 FRBs, respectively. These catalogs, consisting of observed redshifts z^{obs} and dispersion measures DM^{obs} , are described in Section A.1. In essence, we generate host galaxy redshifts, randomly sampled from a distribution scaling with cosmic SFR between redshift $z = 5$ to 15 [adopted from 71], and simulate the observed source redshifts at 10% accuracy, assuming spectroscopic surveys can be used to identify redshifts of host galaxies, e.g. with the James Webb Space Telescope (JWST). As the adopted redshift distribution of FRBs is based on the SFR which drops quickly at high redshifts, we find a negligible number of events above $z = 15$ (a fraction of $< 2 \cdot 10^{-5}$ of all events). However, SFR at such high redshifts is poorly constrained by observations, and early star formation [in agreement with theory and simulations 23, 72] is plausible, which would result in a larger number of high-redshift FRBs than what we consider here.

The corresponding DM^{obs} are computed by adding the IGM, Milky Way, and host galaxy contributions, and taking uncertainties on all of these quantities, as well as the measurement errors, into account. When calculating the IGM contribution we use an input (*true*) reionization history from Kulkarni *et al.* [73] with $\tau = 0.057$ and the midpoint of reionization at $z = 7.3$.

Our analysis pipeline, as described in Section A.2, is based on the free-form method “FlexKnot” [74] where the full reionization history is parameterized by a series of free-moving knots. This algorithm is not informed about the true reionization history and allows us to scan the space of all possible EoR scenarios without assuming a specific functional form or shape, thus avoiding biasing the results. For each such FlexKnot scenario we then model the dispersion measure relation and compute its likelihood given the data. Finally we use Bayesian inference to constrain the parameter space (including the positions and number of knots), recovering the reionization history as well as cosmological parameters.

Results We apply the described method to our synthetic FRB observations and demonstrate that strong reionization constraints can be achieved. Figure 1 shows the constraints on the reionization history, $x_i(z)$, marginalized over individual knot positions and cosmological parameters that have effect on DM (Ω_b/h and Ω_m , see Section A.1.1), and including the CMB polarization constraint on the high-redshift contribution to the total optical depth from $z = 15 - 30$ [$\tau_{15,30}$ from 75, based on Planck18].

In Figure 1 the posterior and prior distributions of $x_i(z)$ are indicated by the orange and purple contours respectively, with

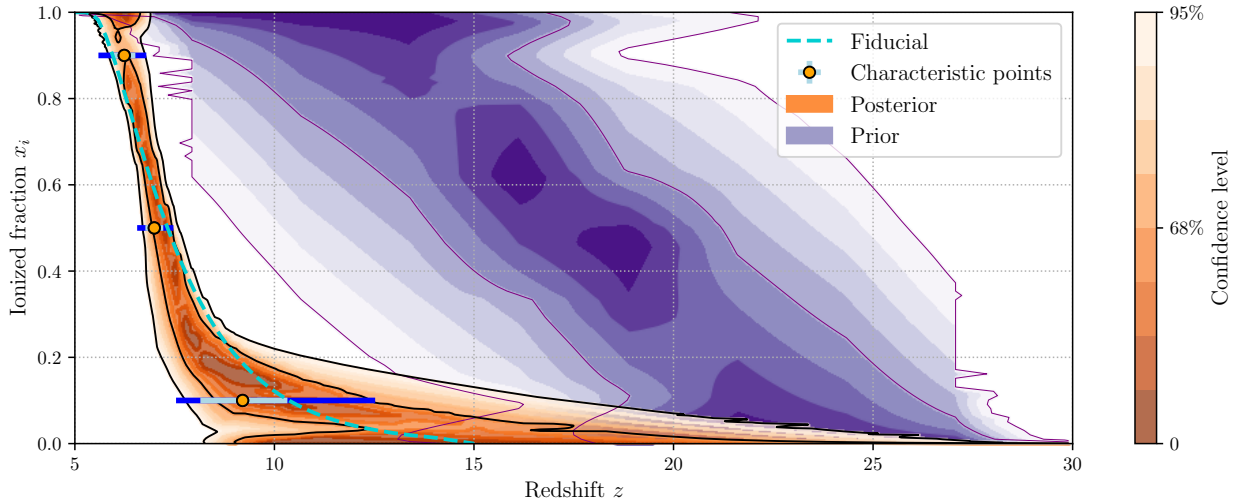


Figure 1: Posterior and prior contours of the reionization history function $x_i(z)$ derived from 1000 localized FRBs distributed proportional to SFR between $z = 5$ and 15 and including the CMB $\tau_{15,30} < 0.019$ [95% 75] limit. The orange and purple areas correspond to the posterior and prior probability density, where the 68 and 95% confidence regions are marked by contour lines. The dashed cyan line indicates the reionization history that was used to generate the synthetic FRB data [from 73]. Additionally, the markers and error bars show the redshifts of start ($x_i = 0.1$), midpoint ($x_i = 0.5$) and end of reionization ($x_i = 0.9$) with 68% (light blue) and 95% (dark blue) confidence intervals.

68% and 95% confidence intervals marked by the solid lines. The posterior provides precise constraints on the reionization history, and encompasses the true reionization history [dashed cyan line, 73] used to generate the data. The prior distribution, shown in purple, follows from assuming a monotonic reionization history and imposing a uniform prior for each individual knot position. This leads to a weak, non-uniform, prior on the interpolated value at any given point, as indicated by the contours.

We find that the FRB data can constrain the reionization history especially well at $z \lesssim 10$ where the vast majority (97%) of the FRB sources in our synthetic catalogue are located. The fact that there is only a small number of FRBs at higher redshifts results in weaker EoR constraints at $z = 10 - 30$. The high-redshift constraints are, to a large part, driven by (i) the enforced monotonicity of the function, (ii) the preference for simpler functions³, and also (iii) by the CMB constraint on early reionization via $\tau_{15,30}$.

With the FlexKnot method we can directly compute posterior probabilities of the start ($x_i = 0.1$), midpoint ($x_i = 0.5$) and end ($x_i = 0.9$) of reionization, which is possible as we have the full shape of $x_i(z)$ for every parameter sample. The results are listed in Table 1 and shown in Figure 1 with the error bars indicating 68% and 95% confidence limits. With 100 FRBs we constrain the end, midpoint and start of reionization to an accuracy of 7%, 6% and 13% respectively at 68% confidence level, achieving a better accuracy of 5%, 3% and 12% respectively for the sample with 1000 FRBs. Note that due to the lack in our catalogue of sources at very high redshift, the 95% constraints on the start of

reionization are asymmetric and the high-redshift tail of the EoR is poorly constrained. We can compare the midpoint limits to the constraints from quasar observations, e.g. Greig & Mesinger [76] use the dark fraction of Lyman α and β forest observations combined with *Planck* measurements to constrain it to $\sim 12\%$ (at 68% confidence level, using physical reionization history models). We see that even 100 observed FRBs will greatly surpass this accuracy.

As can be seen from Figure 1, the constraints on the characteristic points of the EoR are slightly shifted compared to the posterior distribution (orange contours) due to the priors (purple contours) imposed by the flat priors on the knots. We correct for these priors as described in Section A.2.3 so that the constraints on the critical EoR redshifts are obtained with respect to a flat prior on those redshifts.

Marginalizing over all other parameters, including different shapes of reionization histories, we derive posterior probability distributions for the optical depth τ assuming 100 and 1000 FRBs (shown in Figure 2 with blue and orange posteriors respectively) and quote the detailed 68% and 95% limits in Table 1. We find that 100 and 1000 FRBs can constrain the optical depth to 11% and 9% accuracy respectively (68% confidence). Our results for 100 FRBs are competitive with the *Planck*18 measurement of $\tau = 0.0504^{+0.0050}_{-0.0079}$ (68% confidence), while the accuracy for 1000 FRBs surpasses that of *Planck*.

FRBs provide a new probe of τ with a much stronger lower limit than *Planck*'s while the upper bound is weaker due to the scarceness of sources at high redshifts, as can be seen from the asymmetric posterior distribution (Figure 2). This behavior can also be exemplified by considering the low ($z < 10$) and high ($z > 10$) redshift contributions to τ constraints separately: For 100 FRBs we find $\tau_{z < 10} = 0.0513^{+0.0025}_{-0.0025}$ and $\tau_{z > 10} = 0.0042^{+0.0048}_{-0.0042}$ (68% confidence), increasing the data set to 1000 FRBs yields $\tau_{z < 10} = 0.0528^{+0.0011}_{-0.0011}$ and $\tau_{z > 10} = 0.0057^{+0.0050}_{-0.0051}$. While the accuracy in measuring $\tau_{z < 10}$ improves with the sam-

³Note that the preference for simpler functions is an outcome of the weighing by Bayesian evidence. It leads to a slight preference for models with fewer knots if the data provides only weak constraints (“Occam’s razor”), which corresponds to a slight preference for a fast reionization (e.g. when the 2-knot model is preferred) over a more complex reionization history which starts slowly and ends fast (requiring more degrees of freedom). However, this effect becomes very weak if the data are sufficiently constraining (e.g. in Figure 1).

	100 FRBs			1000 FRBs		
	Mean	68%	95%	Mean	68%	95%
Start ($x_i = 0.1$)	$z = 8.8$	+1.1 -1.2	+4.3 -1.8	$z = 9.2$	+1.1 -1.1	+3.3 -1.7
Midpoint ($x_i = 0.5$)	$z = 6.9$	+0.4 -0.4	+1.0 -0.7	$z = 7.0$	+0.2 -0.2	+0.5 -0.4
End ($x_i = 0.9$)	$z = 5.9$	+0.4 -0.4	+0.8 -0.7	$z = 6.2$	+0.3 -0.3	+0.6 -0.6
Optical depth τ	0.0555	+0.0066 -0.0061	+0.0180 -0.0086	0.0584	+0.0055 -0.0054	+0.0141 -0.0074
τ without CMB	0.0606	+0.0085 -0.0086	+0.0263 -0.0120	0.0590	+0.0071 -0.0071	+0.0191 -0.0086

Table 1: Constraints obtained on characteristic points of the reionization history (start, midpoint and end at $x_i = 0.1, 0.5$ and 0.9 respectively), and on the total optical depth τ from FRBs. We include the CMB constraint on $\tau_{15,30}$ [75] which improves the high-redshift accuracy but also provide the τ constraint from FRBs alone in the last row. We list the mean values and 68% and 95% confidence intervals, where the intervals are chosen such that half the exceeding samples lie on each side. The fiducial reionization history used to generate the data has an optical depth of $\tau = 0.057$, and the start, midpoint and end of reionization at redshifts 10.36, 7.32 and 5.95, respectively, all of which lie within the 95% confidence intervals.

ple size, we find that the constraint on $\tau_{z>10}$ is not improved by the additional data.

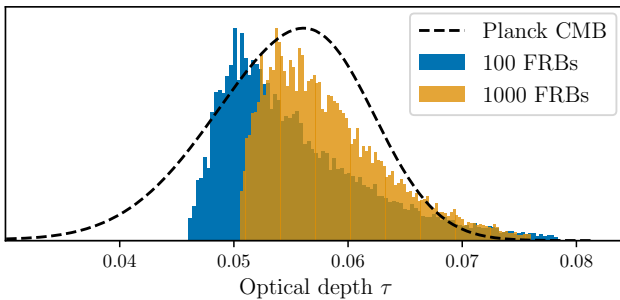


Figure 2: Posterior constraints on the total optical depth τ marginalized over reionization histories as well as cosmological parameters, Ω_b/h and Ω_m . Here we show the constraints from 100 FRBs (blue) and 1000 FRBs (orange), both including the $\tau_{15,30} < 0.019$ limit [75]. We compare the constraints to the Planck18 FlexKnot measurement $\tau = 0.0504^{+0.0050}_{-0.0079}$ (68% confidence, illustrated by the black dashed line) and see that FRBs can significantly improve the optical depth constraint, in particular the lower bound.

An accurate optical depth measurement is not only useful as a probe of reionization, but it will also improve the cosmological constraints obtained from other probes. As an example, Figure 3 shows the limits on the initial amplitude of curvature perturbations A_s measured by *Planck*⁴ (grey contours) which are well known to be degenerate with τ [67]. An independent measurement of τ from FRBs provides tighter constraints on A_s (blue and orange contours in Figure 3). Adding 100 or 1000 FRBs to the *Planck* data reduces relative error in $\ln(10^{10}A_s)$

⁴*Planck* here refers to the combination of CMB temperature and polarization powerspectra, CMB lensing and Baryonic Acoustic Oscillations (BAOs) as used in Planck18, obtained from the Planck Legacy Archive⁵. These constraints assume a tanh reionization history but the A_s constraint is only degenerate with the total optical depth and does not depend on the precise reionization history.

from 0.48% to 0.33% and 0.30% respectively.

Tighter reionization constraints also improve limits on the sum of neutrino masses, $\sum m_\nu$. Future large scale structure surveys such as DESI [77, 78], Euclid [79, 80] and SKA⁶ aim to measure $\sum m_\nu$ but can only achieve their full potential in combination with an independent optical depth measurement [68, 81]. While FRBs alone cannot reach the accuracy of $\sigma_\tau = 0.001$ targeted in Brinckmann *et al.* [68] due to the large uncertainty in $\tau_{z>10}$, they can constrain the lower redshift contribution accurately. Since the latter accounts for the bulk of the optical depth, and provides a lower limit on τ , its accurate measurement in combination with a large scale CMB polarization measurement [e.g. from LiteBIRD or CORE 82, 83] could be sufficient for a detection (lower limit) of $\sum m_\nu$.

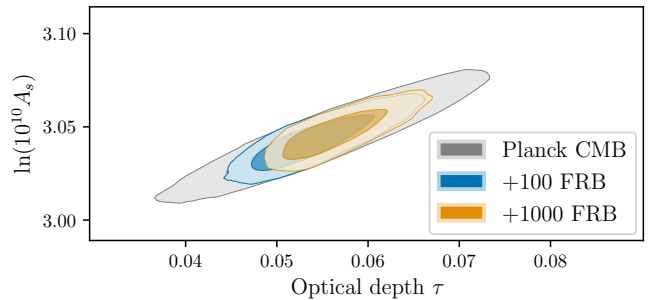


Figure 3: 2D posterior constraints on the primordial power spectrum amplitude A_s and the optical depth τ . Compared to the Planck18 constraints (grey contours), adding a τ constraints from FRBs significantly decreases the uncertainty in A_s . 100 or 1000 FRBs would allow constraints of $\ln 10^{10}A_s = 3.043 \pm 0.010$ or $\ln(10^{10}A_s) = 3.047 \pm 0.009$, respectively, compared to the *Planck* constraint of $\ln(10^{10}A_s) = 3.045 \pm 0.014$ (errors given as standard deviation, correspond to 68% confidence).

Finally, we note that the overall amplitude of the $DM(z)$ relation would in principle allow to constrain cosmological parameters, as it is directly proportional to the baryon density parameter Ω_b/h (and approximately scales with the matter density parameter $\Omega_m^{-0.5}$). However, assuming Λ CDM cosmology, such constraints are degenerate with low-redshift measurements of He-II reionization or the fraction of electrons in the IGM. Therefore, we do not consider such constraints here; these cosmological parameters can be pinned by FRB surveys at lower redshifts [e.g. 13, 19] with experiments such as CHIME [84], HIRAX [85] and ASKAP [86]. We also note that the optical depth constraints are not degenerate with the cosmological parameters Ω_b/h and Ω_m as one might naively expect. This is because the latter two parameters affect the overall amplitude of DM , while optical depth constraints only rely on the shape of the $DM(z)$ function.

Conclusions Using a model-independent approach based on the FlexKnot method and assuming that the number of FRBs scales with the SFR, we have demonstrated the potential of high-redshift FRBs in constraining the reionization history, the CMB optical depth to reionization, the initial amplitude of curvature perturbations and the sum of neutrino masses. Even if the SFR drops quickly at high redshifts, as adopted here, a sample of

⁶<https://www.skatelescope.org/>

100 localized FRBs above $z = 5$ will allow us to surpass the accuracy of the current state-of-the-art CMB experiments and the limits derived from high-redshift quasars. Thus, independent constraints with future FRB surveys have the potential to substantially improve our understanding of reionization and, to some extent, advance our fundamental knowledge.

Acknowledgements We thank A. Boyle, S. Gratton, M. Haehnelt, W. Handley and L. Hergt for helpful discussions. We acknowledge the usage of the DiRAC HPC. AF was supported by the Royal Society University Research Fellowship. DRL acknowledges support from NSF awards AAG-1616042, OIA-1458952 and PHY-1430284. SH acknowledges the support of STFC, via the award of a DTP Ph.D. studentship, and the Institute of Astronomy for a maintenance award.

References

1. Lorimer, D. R., Bailes, M., McLaughlin, M. A., Narkevic, D. J. & Crawford, F. A Bright Millisecond Radio Burst of Extragalactic Origin. *Science* **318**, 777. arXiv: [0709.4301 \[astro-ph\]](#) (Nov. 2007).
2. Spitler, L. G. *et al.* Fast Radio Burst Discovered in the Arecibo Pulsar ALFA Survey. *ApJ* **790**, 101. arXiv: [1404.2934 \[astro-ph.HE\]](#) (Aug. 2014).
3. CHIME/FRB Collaboration *et al.* A second source of repeating fast radio bursts. *Nature* **566**, 235–238. arXiv: [1901.04525 \[astro-ph.HE\]](#) (Jan. 2019).
4. The Chime/Frb Collaboration Andersen, B. Å. C. *et al.* A bright millisecond-duration radio burst from a Galactic magnetar. *Nature* **587**, 54–58 (Nov. 2020).
5. Kumar, P. *et al.* Faint Repetitions from a Bright Fast Radio Burst Source. *ApJ* **887**, L30. arXiv: [1908.10026 \[astro-ph.HE\]](#) (Dec. 2019).
6. Macquart, J.-P. & Johnston, S. On the paucity of fast radio bursts at low Galactic latitudes. *MNRAS* **451**, 3278–3286. arXiv: [1505.05893 \[astro-ph.HE\]](#) (Aug. 2015).
7. Xu, J. & Han, J. L. Extragalactic dispersion measures of fast radio bursts. *Research in Astronomy and Astrophysics* **15**, 1629. arXiv: [1504.00200 \[astro-ph.GA\]](#) (Oct. 2015).
8. Deng, W. & Zhang, B. Cosmological Implications of Fast Radio Burst/Gamma-Ray Burst Associations. *ApJ* **783**, L35. arXiv: [1401.0059 \[astro-ph.HE\]](#) (Mar. 2014).
9. McQuinn, M. Locating the “Missing” Baryons with Extragalactic Dispersion Measure Estimates. *ApJ* **780**, L33. arXiv: [1309.4451 \[astro-ph.CO\]](#) (Jan. 2014).
10. Macquart, J. P. *et al.* A census of baryons in the Universe from localized fast radio bursts. *Nature* **581**, 391–395. arXiv: [2005.13161 \[astro-ph.CO\]](#) (May 2020).
11. Yang, Y.-P. & Zhang, B. Extracting Host Galaxy Dispersion Measure and Constraining Cosmological Parameters using Fast Radio Burst Data. *ApJ* **830**, L31. arXiv: [1608.08154 \[astro-ph.HE\]](#) (Oct. 2016).
12. Fialkov, A. & Loeb, A. Constraining the CMB optical depth through the dispersion measure of cosmological radio transients. *JCAP* **2016**, 004. arXiv: [1602.08130 \[astro-ph.CO\]](#) (May 2016).
13. Zhou, B., Li, X., Wang, T., Fan, Y.-Z. & Wei, D.-M. Fast radio bursts as a cosmic probe? *Phys. Rev. D* **89**, 107303. arXiv: [1401.2927 \[astro-ph.CO\]](#) (May 2014).
14. Gao, H., Li, Z. & Zhang, B. Fast Radio Burst/Gamma-Ray Burst Cosmography. *ApJ* **788**, 189. arXiv: [1402.2498 \[astro-ph.CO\]](#) (June 2014).
15. Walters, A., Weltman, A., Gaensler, B. M., Ma, Y.-Z. & Witzemann, A. Future Cosmological Constraints From Fast Radio Bursts. *ApJ* **856**, 65. arXiv: [1711.11277 \[astro-ph.CO\]](#) (Mar. 2018).
16. Jaroszynski, M. Fast radio bursts and cosmological tests. *MNRAS* **484**, 1637–1644. arXiv: [1812.11936 \[astro-ph.CO\]](#) (Apr. 2019).
17. Madhavacheril, M. S., Battaglia, N., Smith, K. M. & Sievers, J. L. Cosmology with kSZ: breaking the optical depth degeneracy with Fast Radio Bursts. *arXiv e-prints*, arXiv:1901.02418. arXiv: [1901.02418 \[astro-ph.CO\]](#) (Jan. 2019).
18. Wu, Q., Yu, H. & Wang, F. Y. A New Method to Measure Hubble Parameter $H(z)$ Using Fast Radio Bursts. *ApJ* **895**, 33. arXiv: [2004.12649 \[astro-ph.CO\]](#) (May 2020).
19. Hagstotz, S., Reischke, R. & Lilow, R. A new measurement of the Hubble constant using Fast Radio Bursts. *arXiv e-prints*, arXiv:2104.04538. arXiv: [2104.04538 \[astro-ph.CO\]](#) (Apr. 2021).
20. Arcus, W. R., Macquart, J. P., Sammons, M. W., James, C. W. & Ekers, R. D. The fast radio burst dispersion measure distribution. *MNRAS* **501**, 5319–5329. arXiv: [2012.15051 \[astro-ph.CO\]](#) (Mar. 2021).
21. James, C. W. *et al.* The fast radio burst population evolves with the star-formation rate. *arXiv e-prints*, arXiv:2101.07998. arXiv: [2101.07998 \[astro-ph.HE\]](#) (Jan. 2021).
22. Bhandari, S. *et al.* The SURvey for Pulsars and Extragalactic Radio Bursts - II. New FRB discoveries and their follow-up. *MNRAS* **475**, 1427–1446. arXiv: [1711.08110 \[astro-ph.HE\]](#) (Apr. 2018).
23. Naoz, S., Noter, S. & Barkana, R. The first stars in the Universe. *MNRAS* **373**, L98–L102. arXiv: [astro-ph/0604050 \[astro-ph\]](#) (Nov. 2006).
24. Oesch, P. A. *et al.* A Remarkably Luminous Galaxy at $z=11.1$ Measured with Hubble Space Telescope Grism Spectroscopy. *ApJ* **819**, 129. arXiv: [1603.00461 \[astro-ph.GA\]](#) (Mar. 2016).
25. Hashimoto, T. *et al.* The onset of star formation 250 million years after the Big Bang. *Nature* **557**, 392–395. arXiv: [1805.05966 \[astro-ph.GA\]](#) (May 2018).
26. Fialkov, A. & Loeb, A. A Fast Radio Burst Occurs Every Second throughout the Observable Universe. *ApJ* **846**, L27. arXiv: [1706.06582 \[astro-ph.HE\]](#) (Sept. 2017).

27. Hashimoto, T. *et al.* Fast radio bursts to be detected with the Square Kilometre Array. *MNRAS* **497**, 4107–4116. arXiv: [2008.00007 \[astro-ph.HE\]](#) (Aug. 2020).
28. Bochenek, C. D. *et al.* A fast radio burst associated with a Galactic magnetar. *Nature* **587**, 59–62. arXiv: [2005.10828 \[astro-ph.HE\]](#) (Nov. 2020).
29. Metzger, B. D., Berger, E. & Margalit, B. Millisecond Magnetar Birth Connects FRB 121102 to Superluminous Supernovae and Long-duration Gamma-Ray Bursts. *ApJ* **841**, 14. arXiv: [1701.02370 \[astro-ph.HE\]](#) (May 2017).
30. Wadiasingh, Z. & Timokhin, A. Repeating Fast Radio Bursts from Magnetars with Low Magnetospheric Twist. *ApJ* **879**, 4. arXiv: [1904.12036 \[astro-ph.HE\]](#) (July 2019).
31. Wadiasingh, Z. *et al.* The Fast Radio Burst Luminosity Function and Death Line in the Low-twist Magnetar Model. *ApJ* **891**, 82. arXiv: [1910.06979 \[astro-ph.HE\]](#) (Mar. 2020).
32. Beloborodov, A. M. A Flaring Magnetar in FRB 121102? *ApJ* **843**, L26. arXiv: [1702.08644 \[astro-ph.HE\]](#) (July 2017).
33. Popov, S. B. & Postnov, K. A. *Hyperflares of SGRs as an engine for millisecond extragalactic radio bursts in Evolution of Cosmic Objects through their Physical Activity* (eds Harutyunian, H. A., Mickaelian, A. M. & Terzian, Y.) (Nov. 2010), 129–132. arXiv: [0710.2006 \[astro-ph\]](#).
34. Lyubarsky, Y. A model for fast extragalactic radio bursts. *MNRAS* **442**, L9–L13. arXiv: [1401.6674 \[astro-ph.HE\]](#) (July 2014).
35. Turolla, R., Zane, S & Watts, A. L. Magnetars: the physics behind observations. A review. *Reports on Progress in Physics* **78**, 116901. <https://doi.org/10.1088/0034-4885/78/11/116901> (2015).
36. Kaspi, V. M. & Beloborodov, A. M. Magnetars. *ARA&A* **55**, 261–301. arXiv: [1703.00068 \[astro-ph.HE\]](#) (Aug. 2017).
37. Dall’Osso, S., Giacomazzo, B., Perna, R. & Stella, L. Gravitational Waves from Massive Magnetars Formed in Binary Neutron Star Mergers. *ApJ* **798**, 25. arXiv: [1408.0013 \[astro-ph.HE\]](#) (Jan. 2015).
38. Margalit, B., Berger, E. & Metzger, B. D. Fast Radio Bursts from Magnetars Born in Binary Neutron Star Mergers and Accretion Induced Collapse. *ApJ* **886**, 110. arXiv: [1907.00016 \[astro-ph.HE\]](#) (Dec. 2019).
39. Giacomazzo, B., Zrake, J., Duffell, P. C., MacFadyen, A. I. & Perna, R. Producing Magnetar Magnetic Fields in the Merger of Binary Neutron Stars. *ApJ* **809**, 39. arXiv: [1410.0013 \[astro-ph.HE\]](#) (Aug. 2015).
40. Levan, A. J. *et al.* Short gamma-ray bursts in old populations: magnetars from white dwarf-white dwarf mergers. *MNRAS* **368**, L1–L5. arXiv: [astro-ph/0601332 \[astro-ph\]](#) (May 2006).
41. Liu, X. The remnant of neutron star-white dwarf merger and the repeating fast radio bursts. *arXiv e-prints*, arXiv:2002.03693. arXiv: [2002.03693 \[astro-ph.HE\]](#) (Feb. 2020).
42. Zhong, S.-Q. & Dai, Z.-G. Magnetars from Neutron Star-White Dwarf Mergers: Application to Fast Radio Bursts. *ApJ* **893**, 9. arXiv: [2002.11975 \[astro-ph.HE\]](#) (Apr. 2020).
43. Totani, T. Cosmological Fast Radio Bursts from Binary Neutron Star Mergers. *PASJ* **65**, L12. arXiv: [1307.4985 \[astro-ph.HE\]](#) (Oct. 2013).
44. Dokuchaev, V. I. & Eroshenko, Y. N. Recurrent fast radio bursts from collisions of neutron stars in the evolved stellar clusters. *arXiv e-prints*, arXiv:1701.02492. arXiv: [1701.02492 \[astro-ph.HE\]](#) (Jan. 2017).
45. Liu, T., Romero, G. E., Liu, M.-L. & Li, A. Fast Radio Bursts and Their Gamma-Ray or Radio Afterglows as Kerr-Newman Black Hole Binaries. *ApJ* **826**, 82. arXiv: [1602.06907 \[astro-ph.HE\]](#) (July 2016).
46. Zhang, B. Mergers of Charged Black Holes: Gravitational-wave Events, Short Gamma-Ray Bursts, and Fast Radio Bursts. *ApJ* **827**, L31. arXiv: [1602.04542 \[astro-ph.HE\]](#) (Aug. 2016).
47. Mingarelli, C. M. F., Levin, J. & Lazio, T. J. W. Fast Radio Bursts and Radio Transients from Black Hole Batteries. *ApJ* **814**, L20. arXiv: [1511.02870 \[astro-ph.HE\]](#) (Dec. 2015).
48. Abel, T., Bryan, G. L. & Norman, M. L. The Formation of the First Star in the Universe. *Science* **295**, 93–98. arXiv: [astro-ph/0112088 \[astro-ph\]](#) (Jan. 2002).
49. Hosokawa, T., Yoshida, N., Omukai, K. & Yorke, H. W. Protostellar Feedback and Final Mass of the Second-generation Primordial Stars. *ApJ* **760**, L37. arXiv: [1210.3035 \[astro-ph.CO\]](#) (Dec. 2012).
50. Stacy, A. & Bromm, V. The First Stars: A Low-mass Formation Mode. *ApJ* **785**, 73. arXiv: [1307.1798 \[astro-ph.CO\]](#) (Apr. 2014).
51. Hartwig, T., Bromm, V., Klessen, R. S. & Glover, S. C. O. Constraining the primordial initial mass function with stellar archaeology. *MNRAS* **447**, 3892–3908. arXiv: [1411.1238 \[astro-ph.GA\]](#) (Mar. 2015).
52. Haemmerlé, L. *et al.* Formation of the First Stars and Black Holes. *Space Sci. Rev.* **216**, 48. arXiv: [2003.10533 \[astro-ph.GA\]](#) (Apr. 2020).
53. Zhang, B. Fast Radio Burst Energetics and Detectability from High Redshifts. *ApJ* **867**, L21. arXiv: [1808.05277 \[astro-ph.HE\]](#) (Nov. 2018).
54. Agarwal, D. *et al.* Initial results from a real-time FRB search with the GBT. *MNRAS* **497**, 352–360. arXiv: [2003.14272 \[astro-ph.IM\]](#) (Sept. 2020).
55. Hashimoto, T. *et al.* No redshift evolution of non-repeating fast radio burst rates. *MNRAS* **498**, 3927–3945. arXiv: [2008.09621 \[astro-ph.HE\]](#) (Nov. 2020).

56. Zheng, Z., Ofek, E. O., Kulkarni, S. R., Neill, J. D. & Juric, M. Probing the Intergalactic Medium with Fast Radio Bursts. *ApJ* **797**, 71. arXiv: [1409.3244 \[astro-ph.HE\]](#) (Dec. 2014).
57. Caleb, M., Flynn, C. & Stappers, B. W. Constraining the era of helium reionization using fast radio bursts. *MNRAS* **485**, 2281–2286. arXiv: [1902.06981 \[astro-ph.HE\]](#) (May 2019).
58. Linder, E. V. Detecting helium reionization with fast radio bursts. *Phys. Rev. D* **101**, 103019. arXiv: [2001.11517 \[astro-ph.CO\]](#) (May 2020).
59. Lau, A. W. K., Mitra, A., Shafiee, M. & Smoot, G. Constraining HeII reionization detection uncertainties via fast radio bursts. *New Astron.* **89**, 101627 (Nov. 2021).
60. Bhattacharya, M., Kumar, P. & Linder, E. V. Fast Radio Burst Dispersion Measure Distribution as a Probe of Helium Reionization. *arXiv e-prints*, arXiv:2010.14530. arXiv: [2010.14530 \[astro-ph.CO\]](#) (Oct. 2020).
61. Dai, J.-P. & Xia, J.-Q. Reconstruction of Reionization History through Dispersion Measure of Fast Radio Bursts. *arXiv e-prints*, arXiv:2004.11276. arXiv: [2004.11276 \[astro-ph.CO\]](#) (Apr. 2020).
62. Beniamini, P., Kumar, P., Ma, X. & Quataert, E. Exploring the epoch of hydrogen reionization using FRBs. *arXiv e-prints*, arXiv:2011.11643. arXiv: [2011.11643 \[astro-ph.CO\]](#) (Nov. 2020).
63. Zhang, Z. J., Yan, K., Li, C. M., Zhang, G. Q. & Wang, F. Y. Intergalactic Medium Dispersion Measures of Fast Radio Bursts Estimated from IllustrisTNG Simulation and Their Cosmological Applications. *ApJ* **906**, 49. arXiv: [2011.14494 \[astro-ph.CO\]](#) (Jan. 2021).
64. Hashimoto, T. *et al.* Revealing the cosmic reionisation history with fast radio bursts in the era of Square Kilometre Array. *arXiv e-prints*, arXiv:2101.08798. arXiv: [2101.08798 \[astro-ph.CO\]](#) (Jan. 2021).
65. Pagano, M. & Fronenberg, H. Constraining the epoch of reionization with highly dispersed fast radio bursts. *MNRAS* **505**, 2195–2206. arXiv: [2103.03252 \[astro-ph.CO\]](#) (Aug. 2021).
66. Planck Collaboration *et al.* Planck 2018 results. VI. Cosmological parameters. *arXiv e-prints*, arXiv:1807.06209. arXiv: [1807.06209 \[astro-ph.CO\]](#) (July 2018).
67. Hazra, D. K., Paoletti, D., Finelli, F. & Smoot, G. F. Reionization in the dark and the light from Cosmic Microwave Background. *JCAP* **2018**, 016. arXiv: [1807.05435 \[astro-ph.CO\]](#) (Sept. 2018).
68. Brinckmann, T., Hooper, D. C., Archidiacono, M., Lesgourgues, J. & Sprenger, T. The promising future of a robust cosmological neutrino mass measurement. *JCAP* **2019**, 059. arXiv: [1808.05955 \[astro-ph.CO\]](#) (Jan. 2019).
69. Liu, A., Pritchard, J. R., Mortonson, M., Parsons, A. & HERA Collaboration. *Improving Cosmic Microwave Background Constraints with 21cm Cosmology in American Astronomical Society Meeting Abstracts #225* **225** (Jan. 2015), 318.01.
70. Fialkov, A. & Loeb, A. Precise Measurement of the Reionization Optical Depth from the Global 21 cm Signal Accounting for Cosmic Heating. *ApJ* **821**, 59. arXiv: [1601.03058 \[astro-ph.CO\]](#) (Apr. 2016).
71. Behroozi, P., Wechsler, R. H., Hearin, A. P. & Conroy, C. UNIVERSEMACHINE: The correlation between galaxy growth and dark matter halo assembly from $z = 0-10$. *MNRAS* **488**, 3143–3194. arXiv: [1806.07893 \[astro-ph.GA\]](#) (Sept. 2019).
72. Klessen, R. in *Formation of the First Black Holes* (eds Latif, M. & Schleicher, D.) 67–97 (2019).
73. Kulkarni, G. *et al.* Large Ly α opacity fluctuations and low CMB τ in models of late reionization with large islands of neutral hydrogen extending to $z < 5.5$. *MNRAS* **485**, L24–L28. arXiv: [1809.06374 \[astro-ph.CO\]](#) (May 2019).
74. Millea, M. & Bouchet, F. Cosmic microwave background constraints in light of priors over reionization histories. *A&A* **617**, A96. arXiv: [1804.08476 \[astro-ph.CO\]](#) (Sept. 2018).
75. Heinrich, C. & Hu, W. RELIKE: Reionization Effective Likelihood from Planck 2018 Data. *arXiv e-prints*, arXiv:2104.13998. arXiv: [2104.13998 \[astro-ph.CO\]](#) (Apr. 2021).
76. Greig, B. & Mesinger, A. The global history of reionization. *MNRAS* **465**, 4838–4852. arXiv: [1605.05374 \[astro-ph.CO\]](#) (Mar. 2017).
77. Levi, M. *et al.* The DESI Experiment, a whitepaper for Snowmass 2013. *arXiv e-prints*, arXiv:1308.0847. arXiv: [1308.0847 \[astro-ph.CO\]](#) (Aug. 2013).
78. DESI Collaboration *et al.* The DESI Experiment Part I: Science, Targeting, and Survey Design. *arXiv e-prints*, arXiv:1611.00036. arXiv: [1611.00036 \[astro-ph.IM\]](#) (Oct. 2016).
79. Laureijs, R. *et al.* Euclid Definition Study Report. *arXiv e-prints*, arXiv:1110.3193. arXiv: [1110.3193 \[astro-ph.CO\]](#) (Oct. 2011).
80. Amendola, L. *et al.* Cosmology and fundamental physics with the Euclid satellite. *Living Reviews in Relativity* **21**, 2. arXiv: [1606.00180 \[astro-ph.CO\]](#) (Apr. 2018).
81. Boyle, A. & Komatsu, E. Deconstructing the neutrino mass constraint from galaxy redshift surveys. *JCAP* **2018**, 035. arXiv: [1712.01857 \[astro-ph.CO\]](#) (Mar. 2018).
82. Matsumura, T. *et al.* Mission Design of LiteBIRD. *Journal of Low Temperature Physics* **176**, 733–740. arXiv: [1311.2847 \[astro-ph.IM\]](#) (Sept. 2014).
83. Delabrouille, J. *et al.* Exploring cosmic origins with CORE: Survey requirements and mission design. *Journal of Cosmology and Astroparticle Physics* **2018**, 014–014. <https://doi.org/10.1088/1475-7516/2018/04/014> (2018).
84. Bandura, K. *et al.* Canadian Hydrogen Intensity Mapping Experiment (CHIME) pathfinder in Ground-based and Airborne Telescopes V (eds Stepp, L. M., Gilmozzi, R. & Hall, H. J.) **9145** (July 2014), 914522. arXiv: [1406.2288 \[astro-ph.IM\]](#).

85. Newburgh, L. B. *et al.* *HIRAX: a probe of dark energy and radio transients in Ground-based and Airborne Telescopes VI* (eds Hall, H. J., Gilmozzi, R. & Marshall, H. K.) **9906** (Aug. 2016), 99065X. arXiv: [1607.02059](#) [[astro-ph.IM](#)].
86. Johnston, S. *et al.* Science with ASKAP. The Australian square-kilometre-array pathfinder. *Experimental Astronomy* **22**, 151–273. arXiv: [0810.5187](#) [[astro-ph](#)] (Dec. 2008).

A Methodology

Our goal is to predict the accuracy with which future radio surveys will be able to constrain the reionization history and the CMB optical depth⁷ by measuring DMs of high redshift FRBs. In this section we describe the synthetic FRB data catalogue (Section A.1) and the parameter estimation pipeline (Section A.2) used to infer reionization history and cosmological parameters from data.

A.1 Synthetic FRB catalogues

We create a catalog of simulated FRB observations, including redshifts z^{obs} measured from the host galaxy and observed dispersion measures DM^{obs} .

In brief, we generate this catalog as follows. We first create “true” FRB redshifts, z^{true} , by randomly sampling them from a distribution that scales with cosmic star formation rate [SFR, obtained from 71]. We generate two main datasets (with 100 and 1000 FRBs) with z^{true} between 5 and 15, i.e. in the EoR redshift range with 85% of these events falling between redshift $z = 5$ and 8, 12% between 8 and 10, and 3% between 10 and 15. Because the adopted SFR is a rather steep function at high redshifts, only a fraction of $< 2 \cdot 10^{-5}$ of all the events have $z > 15$.

Next, we use z^{true} to generate the observed redshifts, z^{obs} , with an accuracy of 10% (e.g. JWST host galaxy spectroscopy), drawing z^{obs} from a Gaussian distribution $\mathcal{N}(\mu = z^{\text{true}}, \sigma = 0.1z^{\text{true}})$. To compute the corresponding dispersion measures DM^{obs} we compute the mean IGM contribution $\overline{\text{DM}}^{\text{IGM}}$ at z^{true} following the procedure outlined in section A.1.1. We adopt a simulation-based EoR history created by Kulkarni *et al.* [73] with $\tau = 0.057$ and reionization ending around $z = 6$ with the 50% ionization fraction achieved at $z = 7.3$. We also assume the best-fit values of other cosmological parameters from the Planck18 analysis⁸. Synthetic observations DM^{obs} are generated by adding scatter from IGM inhomogeneities, host galaxy, and Milky Way contributions, and then adding an observational measurement error. This approximately corresponds to a Gaussian distribution with uncertainty σ_{DM} , calculated in Equation 5. Repeating this process for each of the generated redshifts

⁷The CMB optical depth is defined as $\tau = c\sigma_T \int_0^{z_{\text{max}}} n_e(z)(1+z)^{-1}H(z)^{-1}dz$, where $z_{\text{max}} \sim 30$, c and σ_T are the speed of light and Thomson scattering cross-section respectively, $n_e(z)$ is the number density of free electrons (from ionized hydrogen and helium) and $H(z)$ is the Hubble parameter.

⁸We use $\Omega_b h^2 = 0.02238$, $\Omega_{\text{cdm}} h^2 = 0.1201$, $H_0 = 67.32$ km/s/Mpc from the CMB power spectra of temperature and E-mode polarization (TT, TE, EE with low E) and including constraints from lensing and Baryon Acoustic Oscillations.

yields a set of synthetic data $D = \{d_1, d_2, \dots\}$ containing pairs of redshifts and dispersion measures $d_i = \{z_i^{\text{obs}}, \text{DM}_i^{\text{obs}}\}$.

A.1.1 DM contributions and uncertainties

The total dispersion measure is commonly decomposed into the contributions from the intergalactic medium (IGM), the host galaxy, and the Milky Way

$$\text{DM}^{\text{tot}} = \text{DM}^{\text{IGM}} + \text{DM}^{\text{host}} + \text{DM}^{\text{MW}}. \quad (1)$$

For each one of these terms we calculate its mean value and the associated uncertainty, $\sigma_{\text{DM}}^{\text{IGM}}$, $\sigma_{\text{DM}}^{\text{host}}$, and $\sigma_{\text{DM}}^{\text{MW}}$ respectively, as described below. In addition, there is a measurement uncertainty, $\sigma_{\text{DM}}^{\text{obs}}$, in the observation of DM^{tot} .

The largest and the most important contribution to DM^{tot} for high redshift FRBs is DM^{IGM} . Owing to the fluctuations in electron density along the line of sight, this quantity is stochastic with the distribution approaching a Gaussian [10], as studied in numerical simulations [16, 63, 87].

For FRBs coming from redshift z , the mean IGM contribution is given by considering a homogeneous distribution of matter (electrons)

$$\overline{\text{DM}}^{\text{IGM}}(z) = \int_0^z \frac{c\bar{n}_e(z')}{H(z')(1+z')^2} dz'. \quad (2)$$

In the above equation, $\bar{n}_e(z')$ is the mean number density of free electrons at redshift z' and $H(z')$ is the Hubble expansion rate. Both quantities can be expressed in terms of the cosmological parameters: $\bar{n}_e(z')$ is proportional to the baryon density parameter today Ω_b and is otherwise determined by the reionization history (Section A.1.2); $H(z')$ depends on the background cosmology via the matter density parameter Ω_m and the Hubble parameter H_0 today (or $h = H_0/(100 \text{ km s}^{-1} \text{ Mpc}^{-1})$). Therefore, we can also write Equation 2 in a more explicit form

$$\overline{\text{DM}}^{\text{IGM}}(z) = \int_0^z \underbrace{\frac{c\bar{n}_e(z')/\Omega_b}{(1+z')^2}}_{\text{EoR dependent}} \underbrace{\frac{\Omega_b}{H_0} \frac{1}{\sqrt{\Omega_m(1+z')^3 + (1-\Omega_m)}}}_{\text{Cosmology dependent}} dz' \quad (3)$$

which shows that DM can be used to constrain cosmological parameters as well as the EoR history. The uncertainty in DM^{IGM} , $\sigma_{\text{DM}}^{\text{IGM}}$, can be approximated by $\sigma_{\text{DM}}^{\text{IGM}} = (0.2/\sqrt{z}) \overline{\text{DM}}^{\text{IGM}}$ ⁹ [5], in agreement with simulations [e.g. 88].

The contributions by the host galaxy and the Milky Way are much smaller compared to that of the IGM. Because the host galaxy contribution DM^{host} is poorly constrained, we assume a conservative estimate of $\text{DM}^{\text{host}} = (200 \pm 100) \text{ pc cm}^{-3}$ in the host galaxy reference frame. The observed contribution of this uncertainty is suppressed by a factor of $(1+z)$. The Milky Way disk can contribute up to $\sim 500 \text{ pc cm}^{-3}$ [see e.g. the CHIME/FRB catalog 89], however this can be accurately estimated from a Galactic electron model, e.g. NE2001 [90], YMW16 [91]. Therefore, we assume we can subtract the MW disk contribution from the observed dispersion measure and include an error of 20 pc cm^{-3} to account for uncertainties in

⁹Note that this approximation yields a lower error for $z \gg z_{\text{reio}}$, so we always consider the maximum error $\text{Max}_{z' \in [0, z]} (\sigma_{\text{DM}}^{\text{IGM}}(z'))$.

the electron model (estimated from the NE2001/YMW16 differences in the CHIME/FRB catalog), and an additional uncertainty of 50 pc cm^{-3} to account for possible contributions from the Milky Way halo [92, 93], combined in quadrature to $\sigma_{\text{DM}}^{\text{MW}} = 54 \text{ pc cm}^{-3}$.

The final contribution to the uncertainty is the measurement error $\sigma_{\text{DM}}^{\text{obs}}$, i.e. how well the FRB arrival time at different frequencies can be measured, calculated following Lorimer *et al.* [94],

$$\sigma_{\text{DM}}^{\text{obs}} = \frac{\nu^3 T_{\text{sys}}}{k G s} \sqrt{\frac{[W_{\text{int}}(1+z)]^2 + (\text{DM } k \Delta\nu / N \nu^3)^2}{2 \Delta\nu^3}}. \quad (4)$$

The uncertainty mainly depends on (i) the pulse width and (ii) the signal to noise ratio. The width is set by two factors: the intrinsic restframe width of an FRB (taken as $W_{\text{int}} = 1 \text{ ms}$), and a small contribution ($\leq 10\%$) due to dispersion smearing (caused by the dispersion of the signal within a frequency channel, effectively broadening the observed pulse width). Sampling and scattering times $\lesssim 10 \text{ ms}$ are negligible. The signal to noise ratio is obtained from radiometer noise considerations [e.g. 95] and depends on the peak spectral flux density s of the signal, and instrument parameters. We compute the former using the most distant localized FRB to date, FRB180924 [96], as a proxy, scaled to higher redshift accounting for luminosity distance and spectral shape, assuming spectral index $\alpha = -1.5$ compatible with the recent results of CHIME/FRB [89]. For comparison, FRB180924 has a higher intrinsic luminosity than about 75% of the CHIME/FRB catalog samples [89]. The instrument parameters are taken to be similar to FAST [97] using a gain $G = 15 \text{ K Jy}^{-1}$, system temperature $T_{\text{sys}} = 35 \text{ K}$, frequency $\nu = 1.4 \text{ GHz}$ with $\Delta\nu = 400 \text{ MHz}$ bandwidth, and $N = 4096$ channels. The scaling constant k is $4.15 \text{ GHz}^2 \text{ ms cm}^3 \text{ pc}^{-1}$.

All these uncertainties on the observed dispersion measure can be combined in quadrature

$$\sigma_{\text{DM}} = \sqrt{(\sigma_{\text{DM}}^{\text{IGM}})^2 + (\sigma_{\text{DM}}^{\text{host}})^2 + (\sigma_{\text{DM}}^{\text{MW}})^2 + (\sigma_{\text{DM}}^{\text{obs}})^2}, \quad (5)$$

assuming that the components are statistically independent normal distributed random variables.

A.1.2 The free electron density

The mean free electron density in Equation 3 is related to the fraction of ionized gas and given by

$$\bar{n}_e(z) = \underbrace{(1 + f_{\text{He}})n_{\text{H}}(1+z)^3 x_i(z)}_{\text{H and He first ionization}} + \underbrace{f_{\text{He}}n_{\text{H}}(1+z)^3 \xi(z)}_{\text{He second ionization}} \quad (6)$$

where $n_{\text{H}}(1+z)^3$ is the mean physical number density of hydrogen atoms (both neutral and ionized) at a given redshift and f_{He} is the helium fraction $f_{\text{He}} = n_{\text{He}}/n_{\text{H}}$. In the above equation we distinguish between the simultaneous hydrogen and first helium reionization at $z > 5$ described by $x_i(z)$, and the second helium reionization at $z < 4$ described by $\xi(z)$. Since the latter only causes a constant shift in DM of high redshift FRBs and can be calibrated out using lower redshift events ($z < 5$), we assume for simplicity that $\xi(z)$ is parameterized by a tanh step function [98] with midpoint $z_{\text{reio}} = 3.5$ and width $\Delta z = 0.5$. For the purpose of generating the synthetic FRB catalogue we use a

simulation-based $x_i(z)$ adopted from Kulkarni *et al.* [73]; however, we use a model-independent parameterization of $x_i(z)$ in the parameter estimation pipeline, as discussed in Section A.2.

Finally note that we treat \bar{n}_e in Equations 3 and 6 as the cosmological mean number density. This is typically slightly higher than the mean number density in the IGM (with the remaining electrons contained mostly in stars). However this enhancement is negligible at the high redshift of interest and the correction factor approaches unity (e.g. Jaroszynski [16] finds 0.964 at $z = 4$ from the Illustris [99] simulation and Takahashi *et al.* [100] report 0.998 at $z = 5$ using IllustrisTNG [101]).

A.2 Parameter estimation pipeline

Our next step is to measure the reionization history and the cosmological parameters directly from the synthetic data. In this process it is essential to avoid biasing the extracted $x_i(z)$ by any specific functional shape, or the model used in the creation of the data set. Therefore, here we adopt a model-independent free-form parameterization of $x_i(z)$. We achieve this by using the FlexKnot [74] method which allows us to sample all possible reionization histories without assuming a pre-defined shape. The method parameterizes the history by a series of free-moving *knots* between which the $x_i(z)$ function is interpolated (Section A.2.1). For any such history we then model the observed dispersion measure DM^{model} and compare it to the observation DM^{obs} to compute the likelihood of that history. In addition to the reionization history we vary relevant cosmological parameters, Ω_b/h and Ω_m , as these affect the dispersion measure. Finally, we use Bayesian inference to constrain the parameter space to recover the “true” reionization history [in our case from 73, which we used to create the synthetic data] as well as the values of the cosmological parameters (Section A.2.3).

A.2.1 Model-independent parameterization of the EoR history

In order to fully harness the power of high-redshift FRBs, we require a parameterization of the reionization history $x_i(z)$. This allows us to take into account the DM and redshift of every measured FRB and combine all information in a Bayesian analysis. However, assuming a specific functional shape for $x_i(z)$ [e.g. 61, 63, assumed tanh and exponential forms] could lead to a bias if the true reionization history significantly deviates from that shape. On the other hand, constraining $x_i(z)$ in fixed redshift bins [as was done by 62, 64] limits the analysis to the binned values and does not make use of all the information contained in an FRB sample (i.e. individual redshift and DM values of each signal). To avoid such biases and limitations, we need to parameterize $x_i(z)$ without restricting the space of possible reionization histories. This issue has been previously dealt with by the CMB community in the context of obtaining CMB optical depth constraints starting with Hu & Holder [102]. Here we adopt the most recent technique from this field, the FlexKnot method which was used to constrain reionization using CMB observations by Millea & Bouchet [74] and is similar to the free-form functional shape constraints on the primordial power spectrum introduced by Vázquez *et al.* [103].

FlexKnot linearly interpolates $x_i(z)$ through a series of N points referred to as “knots”. Each knot n is defined by two

parameters, its position z^n (redshift) and value x_i^n (ionized fraction at this redshift). The knots can be allowed to move left and right (changing z^n) as well as up and down (varying x_i^n). From observations and theoretical considerations we know that the Universe transitions from fully neutral ($x_i = 1$) at high redshifts to fully ionized ($x_i = 0$) at redshift 5-6 [104] and we expect the ionized fraction to monotonically decrease with redshift [105]. Therefore, we fix the value of the first knot to be $x_i^1 = 1$, and the last point $x_i^N = 0$, and require the intermediate points to be monotonic. Note that the endpoints differ from Millea & Bouchet [74] as we only fix the ionized fraction, but not the redshift of the first and last knot.

What makes the FlexKnot method stand out compared to other model-independent techniques such as principle components analysis [102, 106] or interpolation between values at fixed redshifts [*Poly-reion*, 107] is not only that both, the redshifts and ionized fractions of the knots are free to move but also that the number of knots N is a free parameter. This allows the function to be as complex as necessary while values of N higher than warranted by the data will be down-weighted by a lower Bayesian evidence. Note that this implies a slight prior preference towards simpler reionization histories. Given a well-constrained steep reionization history at low redshift, a fast and late start of reionization would be preferred over an early and slow start, as the latter requires more parameters (knots) to describe. In practice however, this is a small effect and only noticeable when there are very few constraints. We run 10 models, starting from $N = 2$ with only start and end point, to $N_{\max} = 11$ with 9 additional, fully movable, knots. Afterwards the evidence becomes negligible and can neglect models with more parameters. Specifically, we find that in the case of just 100 FRBs the simplest model (2 knots) has the highest evidence $Z_1 = 1 \pm 0.25$ with 3 and 4 knot models yielding evidences $Z_3 = 0.57 \pm 0.10$ and $Z_4 = 0.35 \pm 0.06$ respectively. We take models with up to 11 knots into account, where the evidence falls to $Z_{11} = 0.01 \pm 0.001$. For 1000 FRBs however, models with 4 knots achieve the highest evidence ($Z_4 = 1 \pm 0.19$), with other models disfavoured and we cut off again after 11 knots with $Z_{11} = 0.01 \pm 0.001$.

A.2.2 Other reionization history parameterizations

We briefly check what performance of other commonly used parameterizations such as the tanh step-function [63, 98], or the asymmetric exponential function from Dai & Xia [61] and Douspis *et al.* [108]

$$x_i(z) = \begin{cases} 1 - (1 - x_{i,6})(1+z)^3/(1+6)^3 & \text{for } z \leq 6 \\ x_{i,6} \exp(\alpha(6-z)) & \text{for } z > 6. \end{cases} \quad (7)$$

We find that both methods underestimate the optical depth when applied to our synthetic data (with the true value $\tau = 0.057$). For the tanh model we obtain $\tau = 0.0503^{+0.0049}_{-0.0039}$ ($\tau = 0.0518^{+0.0023}_{-0.0019}$) at 95% confidence level, for the exponential one we find $\tau = 0.0513^{+0.0093}_{-0.0055}$ ($\tau = 0.0548^{+0.0032}_{-0.0027}$). Therefore, we caution against assuming a functional form when deriving reionization constraints from data, as such methods work well only if (by chance) the assumed model agrees well with the true reionization history.

A.2.3 Parameter inference

Following Equations 1 to 3 we calculate the dispersion measure $\text{DM}^{\text{model}}(z)$ relation for every set of model parameters θ , which include the number of knots in FlexKnot N , the set of pairs $\{z^n, x_i^n\}$ with $n = 1..N$, and the cosmological parameters Ω_b/H_0 and Ω_m .¹⁰

With this model and the synthetic data set at hand, we use Bayesian analysis to determine the likelihood and compute posterior distributions of all the parameters θ . The likelihood gives the probabilities of observing the i th FRB, $d_i = \{\text{DM}_i^{\text{obs}}, z_i^{\text{obs}}\}$, from a source at true redshift z' with dispersion measure $\text{DM}^{\text{model}}(\theta, z')$, both of which are given by normal distributions¹¹

$$P(d_i|\theta, z') = \mathcal{N}\left(\frac{z_i^{\text{obs}} - z'}{\sigma_z(z')}\right) \mathcal{N}\left(\frac{\text{DM}_i^{\text{obs}} - \text{DM}^{\text{model}}(\theta, z')}{\sigma_{\text{DM}}(z', \text{DM}^{\text{model}}(\theta, z'))}\right). \quad (8)$$

Since the true redshift of the source is unknown we need to marginalize over z' (taking into account the prior¹² on the source redshift $P(z')$) to obtain the likelihood of an observation d_i given just the parameters θ . Finally, we multiply the independent FRB observations to obtain the likelihood for the entire data set $D = \{d_i\}$:

$$P(D|\theta) = \prod_i \int P(d_i|\theta, z')P(z') dz'. \quad (9)$$

We assume flat priors on the positions of the N knots $\{x_n, z_n\}$ in their respective boundaries broadly established by existing reionization constraints (here we very loosely assume z^n to vary between 5 and 30 and x_i^n to be between 0 and 1). For the cosmological parameters we assume Gaussian priors of $\Omega_b/h = 0.0724 \pm 0.0011$ and $\Omega_m = 0.3111 \pm 0.0056$ with mean and variance taken from Planck18.

The fact that we initially impose uniform priors on the knot positions $\{x_n, z_n\}$ implies non-uniform priors on derived parameters such as τ or the midpoint of reionization. When extracting parameter constraints we correct for this effect following Millea & Bouchet [74], adjusting the FlexKnot priors in a minimal way [using maximum entropy priors, 109] to ensure a flat prior on the derived parameter of interest. For instance, to obtain the corrected optical depth posterior distribution $P(\tau|D)$, we just divide the flat FlexKnot position priors $\tilde{\pi}(\{x_n, z_n\})$ by the implicit (undesired) prior at the corresponding value of

¹⁰Computing DM^{model} basically boils down to the homogeneous IGM contribution $\overline{\text{DM}}^{\text{IGM}}$ from Equation 3 and adding the contributions from Equation 1 and uncertainties listed in Equation 5. Or, equivalently, subtracting the non-IGM contributions from observations and comparing to $\overline{\text{DM}}^{\text{IGM}}$.

¹¹Here we model the observational error with a minor approximation, computing the dispersion smearing part from the mean model dispersion measure DM^{model} neglecting the scatter. This significantly accelerates the computation and has a negligible effect (less than 1%) on the (already small) observational error.

¹²This introduces a slight dependence on the true (unknown) FRB distribution. However, the impact of this prior is small and the method does not rely on an accurate prior distribution. We use a simple exponential ze^{-z} distribution [13] as prior and checked that this only shifts the optical depth estimates by $\Delta\tau \lesssim 0.001$ compared to when the true distribution proportional to SFR is used as redshift prior. The uncertainty in the redshift prior might become more relevant for much bigger data sets in the future. However, with bigger data sets we will also be able to constrain the FRB source distribution much more accurately and resolve this question.

$\tau(\{x_n, z_n\})$, $\tilde{\pi}(\tau)$ (obtained by first sampling from the flat knot position priors) and the resulting (non-flat) prior $\pi(\{x_n, z_n\})$ will correspond to a flat prior on τ . We also apply this method to obtain unbiased constraints on the start, midpoint and end of reionization.

As the FlexKnot method provides a full reionization history for every sample of parameters, it is very versatile and one can incorporate additional constraints on $x_i(z)$ from other EoR measurements [e.g. quasars 104] as well as from CMB data by computing the effect of $x_i(z)$ on the CMB power spectrum. We make use of this property here by adding a constraint on the early optical depth between $z = 15$ and 30 , $\tau_{15,30} < 0.019$ (95% confidence), as derived by Heinrich & Hu [75] from the *Planck* CMB data. Note the differentiation between the total τ constraint, and the partial $\tau_{15,30}$ limit: As CMB experiments are more sensitive to ionization at high redshift, constraints on the $z > 15$ optical depth contribution $\tau_{15,30}$ can be derived in addition to the total τ constraint [see e.g. 66, 74, 106, for similar recent constraints].

Finally, we explore the parameter space constrained by FRBs using Nested Sampling [110] with the PolyChord code [111, 112] and the cobaya wrapper [113, 114]. We visualize the distributions using the analysis codes fgivenx [functional posterior, 115] and anesthetic [contour plots, 116]. The generated synthetic data sets as well as the analysis codes used are publicly available¹³. The codes make extensive use of the astropy [117, 118], scipy [119] and numpy [120] python libraries.

References

5. Kumar, P. *et al.* Faint Repetitions from a Bright Fast Radio Burst Source. *ApJ* **887**, L30. arXiv: 1908.10026 [astro-ph.HE] (Dec. 2019).
10. Macquart, J. P. *et al.* A census of baryons in the Universe from localized fast radio bursts. *Nature* **581**, 391–395. arXiv: 2005.13161 [astro-ph.CO] (May 2020).
13. Zhou, B., Li, X., Wang, T., Fan, Y.-Z. & Wei, D.-M. Fast radio bursts as a cosmic probe? *Phys. Rev. D* **89**, 107303. arXiv: 1401.2927 [astro-ph.CO] (May 2014).
16. Jaroszynski, M. Fast radio bursts and cosmological tests. *MNRAS* **484**, 1637–1644. arXiv: 1812.11936 [astro-ph.CO] (Apr. 2019).
61. Dai, J.-P. & Xia, J.-Q. Reconstruction of Reionization History through Dispersion Measure of Fast Radio Bursts. *arXiv e-prints*, arXiv:2004.11276. arXiv: 2004.11276 [astro-ph.CO] (Apr. 2020).
62. Beniamini, P., Kumar, P., Ma, X. & Quataert, E. Exploring the epoch of hydrogen reionization using FRBs. *arXiv e-prints*, arXiv:2011.11643. arXiv: 2011.11643 [astro-ph.CO] (Nov. 2020).
63. Zhang, Z. J., Yan, K., Li, C. M., Zhang, G. Q. & Wang, F. Y. Intergalactic Medium Dispersion Measures of Fast Radio Bursts Estimated from IllustrisTNG Simulation and Their Cosmological Applications. *ApJ* **906**, 49. arXiv: 2011.14494 [astro-ph.CO] (Jan. 2021).
64. Hashimoto, T. *et al.* Revealing the cosmic reionisation history with fast radio bursts in the era of Square Kilometre Array. *arXiv e-prints*, arXiv:2101.08798. arXiv: 2101.08798 [astro-ph.CO] (Jan. 2021).
66. Planck Collaboration *et al.* Planck 2018 results. VI. Cosmological parameters. *arXiv e-prints*, arXiv:1807.06209. arXiv: 1807.06209 [astro-ph.CO] (July 2018).
71. Behroozi, P., Wechsler, R. H., Hearin, A. P. & Conroy, C. UNIVERSEMACHINE: The correlation between galaxy growth and dark matter halo assembly from $z = 0$ –10. *MNRAS* **488**, 3143–3194. arXiv: 1806.07893 [astro-ph.GA] (Sept. 2019).
73. Kulkarni, G. *et al.* Large Ly α opacity fluctuations and low CMB τ in models of late reionization with large islands of neutral hydrogen extending to $z < 5.5$. *MNRAS* **485**, L24–L28. arXiv: 1809.06374 [astro-ph.CO] (May 2019).
74. Millea, M. & Bouchet, F. Cosmic microwave background constraints in light of priors over reionization histories. *A&A* **617**, A96. arXiv: 1804.08476 [astro-ph.CO] (Sept. 2018).
75. Heinrich, C. & Hu, W. RELIKE: Reionization Effective Likelihood from Planck 2018 Data. *arXiv e-prints*, arXiv:2104.13998. arXiv: 2104.13998 [astro-ph.CO] (Apr. 2021).
87. Batten, A. J. *et al.* The Cosmic Dispersion Measure in the EAGLE Simulations. *arXiv e-prints*, arXiv:2011.14547. arXiv: 2011.14547 [astro-ph.CO] (Nov. 2020).
88. Jaroszyński, M. FRBs: the Dispersion Measure of Host Galaxies. *Acta Astron.* **70**, 87–100. arXiv: 2008.04634 [astro-ph.GA] (June 2020).
89. Rafiei-Ravandi, M. *et al.* CHIME/FRB Catalog 1 results: statistical cross-correlations with large-scale structure. *arXiv e-prints*, arXiv:2106.04354. arXiv: 2106.04354 [astro-ph.CO] (June 2021).
90. Cordes, J. M. & Lazio, T. J. W. NE2001.I. A New Model for the Galactic Distribution of Free Electrons and its Fluctuations. *arXiv e-prints*, astro-ph/0207156. arXiv: astro-ph/0207156 [astro-ph] (July 2002).
91. Yao, J. M., Manchester, R. N. & Wang, N. A New Electron-density Model for Estimation of Pulsar and FRB Distances. *ApJ* **835**, 29. arXiv: 1610.09448 [astro-ph.GA] (Jan. 2017).
92. Yamasaki, S. & Totani, T. The Galactic Halo Contribution to the Dispersion Measure of Extragalactic Fast Radio Bursts. *ApJ* **888**, 105. arXiv: 1909.00849 [astro-ph.HE] (Jan. 2020).
93. Keating, L. C. & Pen, U.-L. Exploring the dispersion measure of the Milky Way halo. *MNRAS* **496**, L106–L110. arXiv: 2001.11105 [astro-ph.GA] (July 2020).
94. Lorimer, D. R., Karastergiou, A., McLaughlin, M. A. & Johnston, S. On the detectability of extragalactic fast radio transients. *MNRAS* **436**, L5–L9. arXiv: 1307.1200 [astro-ph.HE] (Nov. 2013).
95. Condon, J. J. & Ransom, S. M. *Essential Radio Astronomy* (2016).

¹³<https://github.com/Stefan-Heimersheim/FlexKnotFRB>

96. Bannister, K. W. *et al.* A single fast radio burst localized to a massive galaxy at cosmological distance. *Science* **365**, 565–570. arXiv: [1906.11476 \[astro-ph.HE\]](#) (Aug. 2019).
97. Nan, R. *et al.* The Five-Hundred Aperture Spherical Radio Telescope (fast) Project. *International Journal of Modern Physics D* **20**, 989–1024. arXiv: [1105.3794 \[astro-ph.IM\]](#) (Jan. 2011).
98. Lewis, A. Cosmological parameters from WMAP 5-year temperature maps. *Phys. Rev. D* **78**, 023002. arXiv: [0804.3865 \[astro-ph\]](#) (July 2008).
99. Vogelsberger, M. *et al.* Properties of galaxies reproduced by a hydrodynamic simulation. *Nature* **509**, 177–182. arXiv: [1405.1418 \[astro-ph.CO\]](#) (May 2014).
100. Takahashi, R., Ioka, K., Mori, A. & Funahashi, K. Statistical modelling of the cosmological dispersion measure. arXiv: [2010.01560 \[astro-ph.CO\]](#) (Oct. 2020).
101. Springel, V. *et al.* First results from the IllustrisTNG simulations: matter and galaxy clustering. *MNRAS* **475**, 676–698. arXiv: [1707.03397 \[astro-ph.GA\]](#) (Mar. 2018).
102. Hu, W. & Holder, G. P. Model-independent reionization observables in the CMB. *Phys. Rev. D* **68**, 023001. arXiv: [astro-ph/0303400 \[astro-ph\]](#) (July 2003).
103. Vázquez, J. A., Bridges, M., Hobson, M. P. & Lasenby, A. N. Model selection applied to reconstruction of the Primordial Power Spectrum. *JCAP* **2012**, 006. arXiv: [1203.1252 \[astro-ph.CO\]](#) (June 2012).
104. McGreer, I. D., Mesinger, A. & D’Odorico, V. Model-independent evidence in favour of an end to reionization by $z \approx 6$. *MNRAS* **447**, 499–505. arXiv: [1411.5375 \[astro-ph.CO\]](#) (Feb. 2015).
105. Furlanetto, S. R. & Loeb, A. Is Double Reionization Physically Plausible? *ApJ* **634**, 1–13. arXiv: [astro-ph/0409656 \[astro-ph\]](#) (Nov. 2005).
106. Heinrich, C. & Hu, W. Does Planck 2015 polarization data favor high redshift reionization? *Phys. Rev. D* **98**, 063514. arXiv: [1802.00791 \[astro-ph.CO\]](#) (Sept. 2018).
107. Hazra, D. K. & Smoot, G. F. Witnessing the reionization history using Cosmic Microwave Background observation from Planck. *JCAP* **2017**, 028. arXiv: [1708.04913 \[astro-ph.CO\]](#) (Nov. 2017).
108. Douspis, M., Aghanim, N., Ilić, S. & Langer, M. A new parameterization of the reionisation history. *A&A* **580**, L4. arXiv: [1509.02785 \[astro-ph.CO\]](#) (Aug. 2015).
109. Handley, W. & Millea, M. Maximum-Entropy Priors with Derived Parameters in a Specified Distribution. *Entropy* **21**, 272. arXiv: [1804.08143 \[math.ST\]](#) (Mar. 2019).
110. Skilling, J. *Nested Sampling in Bayesian Inference and Maximum Entropy Methods in Science and Engineering: 24th International Workshop on Bayesian Inference and Maximum Entropy Methods in Science and Engineering* (eds Fischer, R., Preuss, R. & Toussaint, U. V.) **735** (Nov. 2004), 395–405.
111. Handley, W. J., Hobson, M. P. & Lasenby, A. N. polychord: nested sampling for cosmology. *MNRAS* **450**, L61–L65. arXiv: [1502.01856 \[astro-ph.CO\]](#) (June 2015).
112. Handley, W. J., Hobson, M. P. & Lasenby, A. N. POLYCHORD: next-generation nested sampling. *MNRAS* **453**, 4384–4398. arXiv: [1506.00171 \[astro-ph.IM\]](#) (Nov. 2015).
113. Torrado, J. & Lewis, A. *Cobaya: Bayesian analysis in cosmology* Oct. 2019. ascl: [1910.019](#).
114. Torrado, J. & Lewis, A. Cobaya: Code for Bayesian Analysis of hierarchical physical models. *arXiv e-prints*, arXiv:2005.05290. arXiv: [2005.05290 \[astro-ph.IM\]](#) (May 2020).
115. Handley, W. fgivenx: A Python package for functional posterior plotting. *The Journal of Open Source Software* **3**, 849. arXiv: [1908.01711 \[astro-ph.IM\]](#) (Aug. 2018).
116. Handley, W. anesthetic: nested sampling visualisation. *The Journal of Open Source Software* **4**, 1414. arXiv: [1905.04768 \[astro-ph.IM\]](#) (May 2019).
117. Astropy Collaboration *et al.* Astropy: A community Python package for astronomy. *A&A* **558**, A33. arXiv: [1307.6212 \[astro-ph.IM\]](#) (Oct. 2013).
118. Astropy Collaboration *et al.* The Astropy Project: Building an Open-science Project and Status of the v2.0 Core Package. *AJ* **156**, 123. arXiv: [1801.02634 \[astro-ph.IM\]](#) (Sept. 2018).
119. Virtanen, P. *et al.* SciPy 1.0: Fundamental Algorithms for Scientific Computing in Python. *Nature Methods* **17**, 261–272 (2020).
120. Harris, C. R. *et al.* Array programming with NumPy. *Nature* **585**, 357–362. <https://doi.org/10.1038/s41586-020-2649-2> (Sept. 2020).